Research Article

Xu Deng, Weiwei Wu*, Shuang Ding, Yanjun Zhang, and Binquan Shi

Investigation of different structures of screw extruders on the flow in direct ink writing SiC slurry based on LBM

https://doi.org/10.1515/phys-2023-0156
received May 04, 2023; accepted November 20, 2023

Abstract: Direct ink writing provides a new method for ceramic material forming. The single-screw extruder is used here to extrude viscous SiC slurry. Because the flow mechanism of ceramic slurry in the slurry direct writing extrusion device is unclear, lattice Boltzmann method (LBM) is used to analyze the flow process of ceramic slurry in the extrusion device. In this study, three different types of special-shaped, single-screw extruders (constant depth variable pitch screw, variable depth constant pitch screw, and variable depth variable pitch screw) are investigated to explore the effects of the shapes on the flow process. Compared with the traditional single-screw extruder, more attention should be paid to the difference in the flow channel. The non-Newtonian rheological model of SiC slurry is built, then the LBM for the non-Newtonian slurry is introduced and used to conduct the simulations based on the aforementioned three different cases. The results show that the effect of constant depth and variable pitch screw on the flow of ceramic slurry is the least and the flow of ceramic slurry in variable depth and variable pitch screw is the most complex.

Keywords: 3D printing, LBM, ceramic slurry, flow analysis, special-shaped screw

Nomenclature

$\boldsymbol{D}_{\mathrm{II}}$	the second variable of the strain rate tensor
$\boldsymbol{e}_a$	discrete speed of the D2Q9 model
$f_a^{\mathbf{eq}}$	equilibrium distribution function
$\boldsymbol{r}$	position vector
$\boldsymbol{S}_{\alpha\beta}$	strain rate tensor
$\boldsymbol{u}$	velocity vector
w_a	weight factor
ρ	density
τ	relaxation time
μ	dynamic viscosity
δr	space displacement
δt	time displacement
ω	collision frequency

1 Introduction

Ceramic materials have many advantages, such as high melting point, high hardness, good wear resistance, and chemical stability, which have been widely used in aerospace, electronic manufacturing, biomedical, and other fields [1,2]. There are many processing methods for molding ceramic parts. Injection molding is the most traditional processing method. When it is used to process a workpiece with complex geometry, the complex process and long processing cycle are required and the molding will fail [3]. As a new technology of intelligent manufacturing, additive manufacturing (AM) provides a new way of processing the ceramic parts [4–8]. Direct ink writing (DIW) is an extrusion method of AM, which has been one of the mainstream processes for molding ceramic materials by AM technologies in recent years. It can realize complex ceramic parts with complex geometries [9–15].

Generally speaking, DIW requires good material fluidity, but the viscosity of the ceramic slurry is relatively high, and traditional equipment (needle-cylinder device) cannot effectively transport it. Therefore, a single-screw extruder is used here to improve transportation performance [16]. The depth and pitch screw are the main structural parameters. To understand the effect of two parameters on the ceramic flow, three different types of special-shaped, single-screw

* **Corresponding author: Weiwei Wu,** School of Mechanical Engineering, Yangzhou University, 225009, Yangzhou, China, e-mail: wuweiwei@yzu.edu.cn
Xu Deng, **Shuang Ding**, **Yanjun Zhang:** School of Mechanical Engineering, Yangzhou University, 225009, Yangzhou, China
Binquan Shi: Jiangsu Yongsheng Air Conditioner Co., Ltd., 225400, Taizhou, China

extruders (constant depth variable pitch screw, variable depth constant pitch screw, and variable depth variable pitch screw) [17–19] are analyzed, respectively [20].

To conduct the flow analysis, many common methods can be adopted, such as experiments and numerical simulation. For the experiment method, a sensor is used to install on the extruder. It is difficult to find an appropriate sensor with good wet-skid corrosion and impact resistance. Therefore, the experimental method is not recommended here. Numerical simulation has become a more suitable alternative method. When the problems of fluid mechanics cannot be solved by existing theories, the finite element method and the finite difference method have helped solve a lot of practical problems. Lattice Boltzmann method (LBM) is a fluid calculation and modeling method different from traditional numerical methods, which is a simple algorithm, easy programming, has high parallelism, and can handle complex boundary conditions. Therefore, the LBM based on MATLAB programming is used here to analyze the ceramic slurry flow. LBM can process not only the simple flow but also the complex situation, such as the complex rheological behavior. David *et al.* [21] made an impedance model of human arterial blood flow using MATLAB. Ponalagusamy and Manchi [22] conducted a flow analysis of non-Newtonian fluid in arteries with mild stenosis. Siddiqa *et al.* [23] analyzed the power-law flow in a narrow tube by LBM. Bouzit *et al.* [24] studied the rheological characteristics and curvature radius effect of non-Newtonian fluid flow in a curved square pipe. Bisht and Patil [25] evaluated the applicability of the MRT LBM for ordinary non-Newtonian fluids and conducted the relevant case validation. Khabazi *et al.* [26] used MRT LBM to simulate and analyze the Bingham fluid inside a two-dimensional channel and considered several factors that could affect the flow. Based on the aforementioned cases, LBM can also be used to analyze non-Newtonian ceramic flow in the single-screw extruder.

The main objective of this study is to analyze the differences in flow during slurry transportation between three types of special-shaped single screws and traditional single-screw extruders. A LBM suitable for non-Newtonian fluids such as ceramic slurry is proposed and used for simulation analysis. Finally, the simulation results of the three were compared for analysis and discussion.

This article is organized as follows. In Section 2, the rheological model is built by testing the rheological behavior of ceramic slurry. In Section 3, the LBM for non-Newtonian ceramic slurry flow is proposed. In Section 4, the numerical results are obtained by analyzing the flow in three different types of profiled single-screw extruders. Finally, the simulation results are discussed and concluded.

2 Rheological behaviors

2.1 Preparation of ceramic slurry

Raw materials contained an average particle size of 0.5 μm, 60 wt% SiC powders, 20 wt% carbon powder with an average particle size of 250 nm, 5 wt% polyvinyl alcohol, and 20 wt% water. First, polyvinyl alcohol and water were mixed to prepare the adhesive solution. Then, the ceramic powder and carbon powder were added into the adhesive solution and centrifuged at 1,000 rpm for 3 minutes to completely dissolve them. Finally, the ceramic slurry with a solid content of 80% was obtained for subsequent experiments [27–29].

2.2 Rheological test and result

Based on the rheological test result, the Williamson model and the Sisko model are considered the most possible models for the slurry. In Figure 1, the comparison is

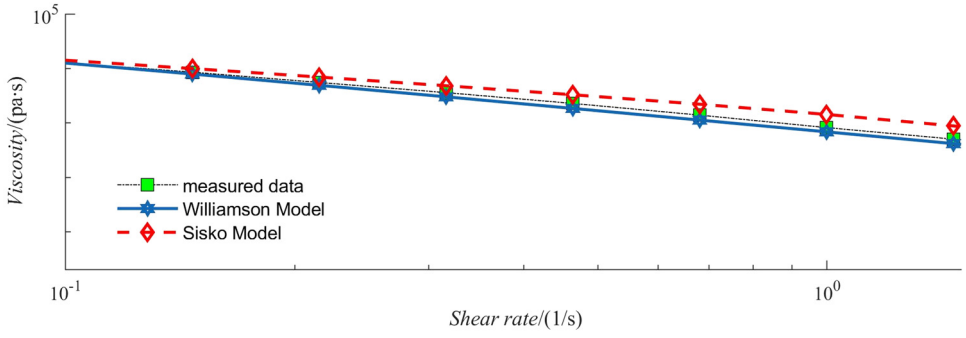

Figure 1: Nonlinear fitting results.

made between the Williamson model, the Sisko model, and the actual measured data.

It can be found that the fitting curve coincidence between the Williamson model [30] and the measured data is higher than that of the Sisko model [31]. Table 1 shows the specific equations and parameters of the Williamson model and the Sisko model. The *R*-square can indicate the quality of the fitting result. The closer it is to 1, the better the fitting result is. Therefore, the Williamson model is more suitable for the following simulation.

3 LBM for non-newtonian SiC slurry flow

A complete lattice Boltzmann model generally consists of three parts: discrete velocity model, equilibrium distribution function, and evolution equation of distribution function.

The discrete speed of the D2Q9 model [32,33] can be expressed as:

$$\boldsymbol{e_a} = \begin{cases} (0,0) & a = 0 \\ c\left(\cos\left[(a-1)\frac{\pi}{2}\right], \sin\left[(a-1)\frac{\pi}{2}\right]\right) & a = 1,2,3,4 \\ \sqrt{2}c\left(\cos\left[(2a-1)\frac{\pi}{4}\right], \sin\left[(2a-1)\frac{\pi}{4}\right]\right) & a = 5,6,7,8 \end{cases} \quad (1)$$

where $c = \delta_x/\delta_t$, $\delta_x$is the grid step size and δ_t is the time step size, both of them are always taken as 1, so $c = 1$. Generally, the step sizes in the x- and y-directions of the grid are both taken as 1, so $c = 1$.

Under the condition of a stationary boundary, a standard reflection form was adopted. When the boundary velocity has been determined, Zou and He [34] proposed a new non-equilibrium-state reflection form as a new boundary treatment method, which does not require the boundary to be determined as a solid boundary.

The evolution equation of the discrete distribution function in the D2Q9 model is as follows:

Table 1: Fitting results of different flow models

Model	Equation	*R*-square	Adjusted *R*-square
Williamson	$\mu = 1405.05/[1 + (59.58\dot{\gamma})^{1.303}]$	0.999	0.9989
Sisko	$\mu = -6{,}568 + 7{,}377\dot{\gamma}^{-0.12145}$	0.9125	0.9060

$$f_a(\boldsymbol{r} + \delta r, t + \delta t) - f_a(\boldsymbol{r}, t) = -\omega[f_a(\boldsymbol{r}, t) - \boldsymbol{f_a^{eq}}(\boldsymbol{r}, t)], \quad (2)$$

where ω is the collision frequency, $f_a^{\mathbf{eq}}$ is the equilibrium distribution function, $\boldsymbol{r}$ is the position vector, t is the time, δr is referred to as the space displacement, and δt is referred to as the time displacement.

The formula for the relaxation parameter ω is as follows:

$$\omega = \frac{1}{\tau} = \frac{2\rho}{6\mu + \rho}, \quad (3)$$

where τ is the relaxation time, μ is the dynamic viscosity, and ρ is the density.

For D2Q9 model, the sound velocity of the lattice $c_s = \boldsymbol{e_a}/\sqrt{3}$, we can know from Eq. (1) that $c_s^2 = 1/3$.

In the D2Q9 model, the equilibrium distribution function can be expressed as:

$$\boldsymbol{f_a^{eq}} = \rho \boldsymbol{w_a}\left[1 + \frac{\boldsymbol{e_a}\cdot\boldsymbol{u}}{c_s^2} + \frac{(\boldsymbol{e_a}\cdot\boldsymbol{u})^2}{2c_s^4} - \frac{\boldsymbol{u}^2}{2c_s^2}\right], \quad (4)$$

where w_a is the weight factor, u is the velocity vector, and the value of the weight factor is described in detail as $w_0 = 4/9$, $w_1 = w_2 = w_3 = w_4 = 1/9$, and $w_5 = w_6 = w_7 = w_8 = 1/36$.

When $c_s^2 = 1/3$ is known, Eq. (4) can be simplified as:

$$\boldsymbol{f_a^{eq}} = \rho \boldsymbol{w_a}\left[1 + 3\boldsymbol{e_a}\cdot\boldsymbol{u} + \frac{9}{2}(\boldsymbol{e_a}\cdot\boldsymbol{u})^2 - \frac{3}{2}\boldsymbol{u}^2\right]. \quad (5)$$

To recover the macro equation, the equilibrium distribution function needs to satisfy the following equations:

$$\rho = \sum_{a=0}^{8} f_a, \quad (6)$$

$$\boldsymbol{u} = \frac{1}{\rho}\sum_{a=0}^{8} f_a \boldsymbol{e_a}. \quad (7)$$

For the non-Newtonian fluid, its shear rate changes with viscosity, and its relaxation time also changes. Therefore, the strain rate tensor shall be derived as:

$$S_{\alpha\beta} = -\frac{1}{2\rho\tau c_S^2}\sum_{i=0}^{8} e_{i\alpha}e_{i\beta}(f_i - f_i^{\mathrm{eq}}). \quad (8)$$

The second variable of the strain rate tensor can be calculated by the following equation:

$$D_{\mathrm{II}} = \sum_{\alpha,\beta=1}^{l} S_{\alpha\beta}S_{\alpha\beta}. \quad (9)$$

The shear rate is derived from the following equation:

$$\dot{\gamma} = \sqrt{2D_{\mathrm{II}}}. \quad (10)$$

The rheological equation of the Williamson model is expressed as:

$$\mu = \mu_0/[1 + (\lambda_w\dot{\gamma})^n]. \quad (11)$$

Based on Eqs. (10) and (11), the dynamic viscosity can be obtained, and then, the next iteration can be conducted.

MATLAB software is used here for numerical simulation, and the specific steps are as follows:

1. Units shall be converted according to the Reynolds number. Then, the specific physical quantities are transformed into dimensionless numbers for numerical simulation. Define the initial calculation parameters, such as lattice number, entrance velocity, initial relaxation parameter, and initial density.
2. Set the initial distribution function and the equilibrium distribution function. Initially, the distribution function is the same as the equilibrium distribution function, and its expression is shown in Eq. (5).
3. Due to the simulation of the special-shaped, single-screw extruder, the flow channel should be designed according to different types of screws.
4. In each step, the calculation using lattice Boltzmann requires two parts, namely, the collision process and the migration process. The LBGK approximate equation is selected for the design program, so the collision equation is as follows:

$$f_a(r, t + \delta t) = f_a(r, t) - \omega[f_a(r, t) - \boldsymbol{f}_{\boldsymbol{a}}^{\mathbf{eq}}(r, t)]. \quad (12)$$

The migration equation is as follows:

$$f_a(r + \delta r, t + \delta t) = f_a(r, t). \quad (13)$$

5. According to Eq. (11), the dynamic viscosity of the ceramic slurry is constantly changing because it belongs to non-Newtonian fluids, and new viscosity and relaxation parameters need to be calculated for the next iteration.
6. Conduct non-equilibrium bound boundary treatment.
7. Generate a mobile cloud image through the function of the image.

4 Effect of different-shaped single screw on ceramic slurry flow

In the current work, three types of special-shaped single screws have been considered: constant depth variable pitch screw, variable depth constant pitch screw, and variable depth variable pitch screw. The aim is to find the effect of two parameters (depth and pitch screw) on the ceramic flow in DIW technology.

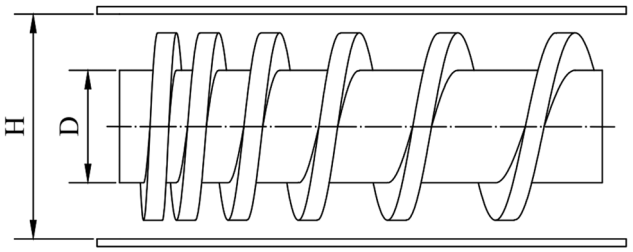

Figure 2: Engineering drawing of constant depth variable pitch screw.

4.1 Constant depth variable pitch screw

When a constant depth variable pitch screw is used, it is not necessary to consider the depth change compared with the traditional screw extruder. The flow channel of the screw can be considered an isosceles trapezoid on the x–z-section. The structure and the flow channel are shown in Figures 2 and 3. The width of the channel inlet is 10 mm, and the x–y-section at z = 5 mm is taken for analysis, while the y–z-section at x = 50 mm is taken for analysis. The flow in both the x–y- and y–z-sections is analyzed with a constant. In the simulation, the involved parameters are set as follows. The grid point is set to 200 × 50. When the difference in the velocities of two adjacent iterations is smaller than 10^{-6}, the simulation is finished. The same conditions are adopted in the following situations.

When simulating the flow in the x–y-section, the inlet velocity is represented by a parabola, with a maximum value of 0.5 m/s and a minimum value of 0 m/s, the entrance speed here is set based on the actual situation, and the same conditions are adopted in the following situations. The cloud diagram is shown in Figure 4(a); the orange represents the high-velocity area, and the blue corresponds to the low-velocity area. As shown in Figure 4(b) and (c), the velocity u_x in the x-direction shows a trend of first increasing and then

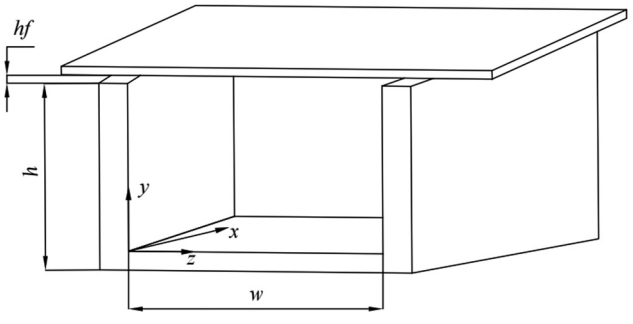

Figure 3: Flow channel of constant depth variable pitch screw.

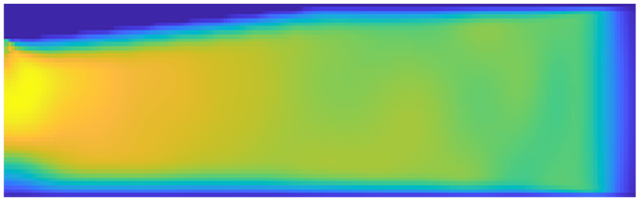

(a)

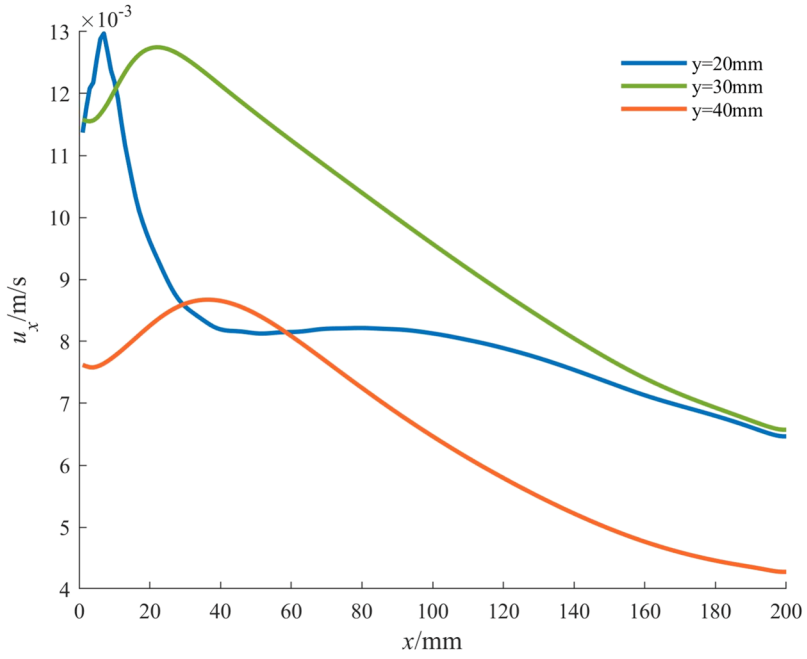

(b)

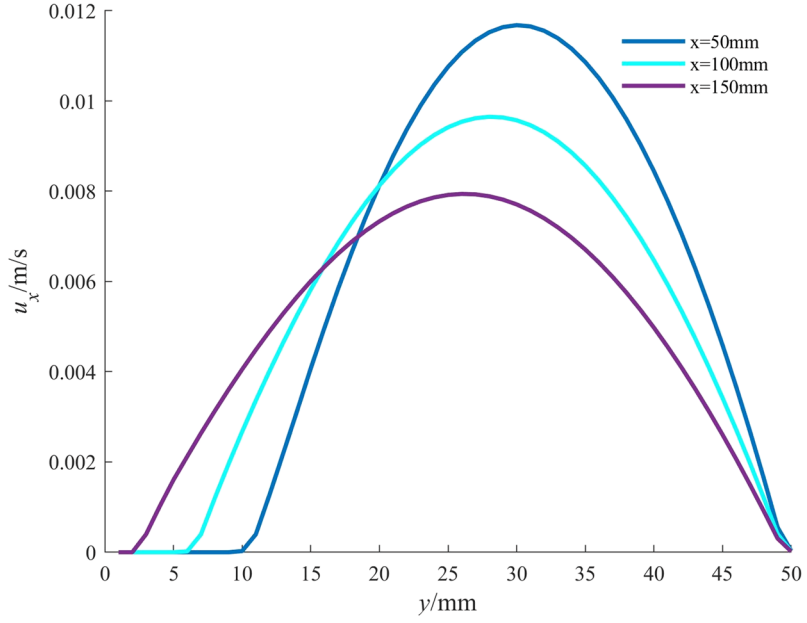

(c)

Figure 4: Simulation results of constant depth variable pitch screw in the *x*–*y*-direction: (a) velocity distribution diagram of a constant depth variable pitch screw, (b) velocity distribution of u_x in the *x*-direction, (c) velocity distribution of u_x in the *y*-direction, (d) velocity distribution of u_y in the *x*-direction, and (e) velocity distribution of u_y in the *y*-direction.

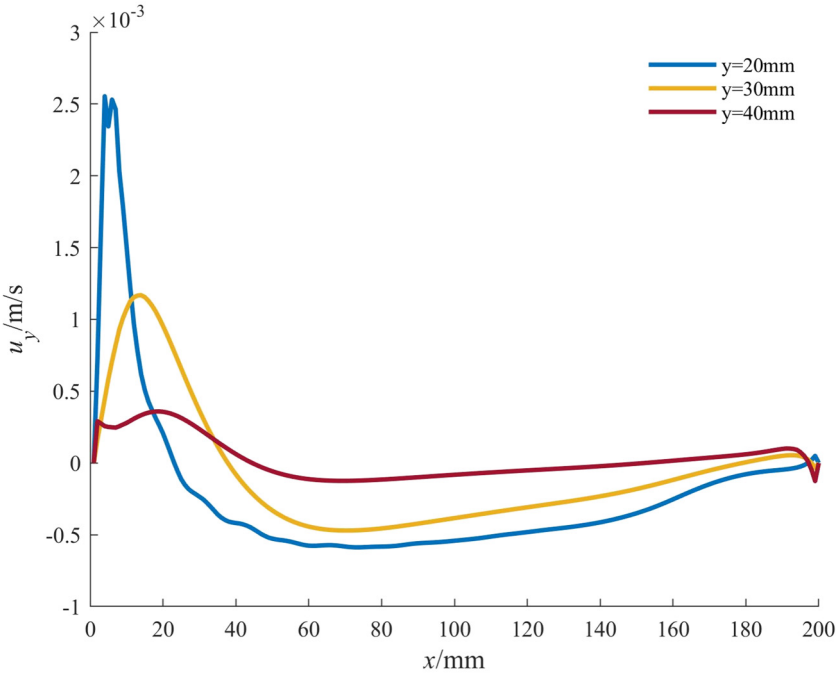

(d)

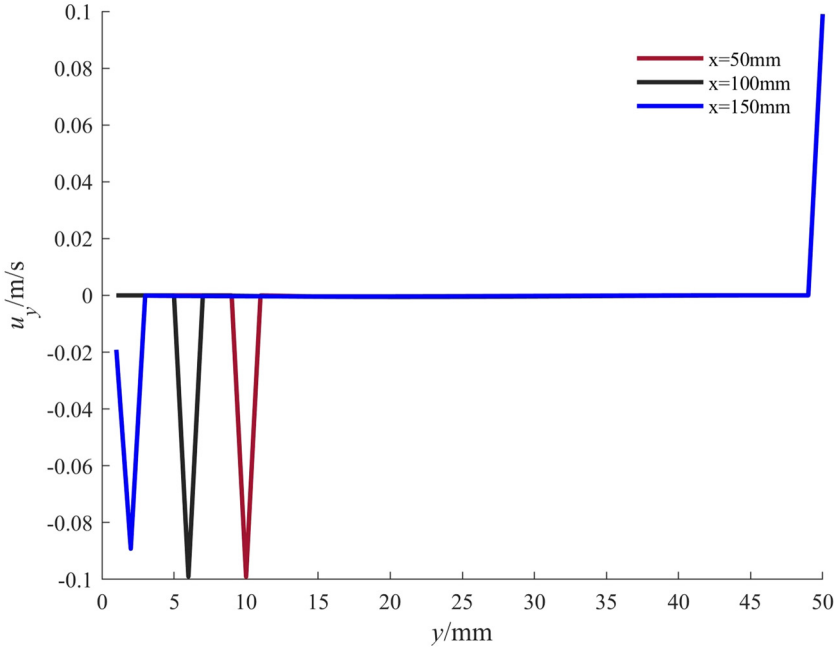

(e)

Figure 4: (*Continued*)

slowly decreasing, the reason for the appearance of this pattern is probably due to the gradually expanding opening of the flow channel, but due to the small initial diameter, it has an impact on the flow. While the velocity curve in the *y*-direction shows a parabolic shape with an opening downward. As shown in Figure 4(d) and (e), the velocity u_y in the *x*-direction shows a trend of first increasing, then decreasing, and finally slowly increasing. The velocity u_y in the *y*-direction first decreases and then increases, remaining unchanged at a velocity of 0 and finally showing an upward trend.

When the flow in the *y*–*z*-section is investigated, the inlet velocity is represented by a parabola, with a maximum value of 0.2 m/s and a minimum value of 0 m/s. The value of the inlet velocity here is selected based on

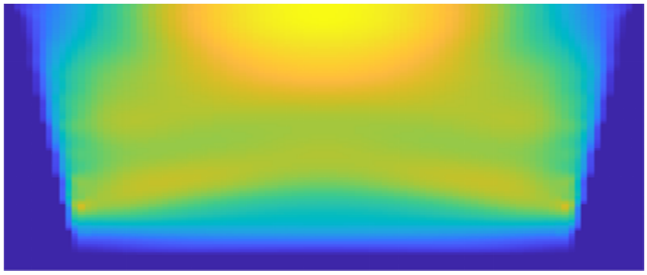

(a)

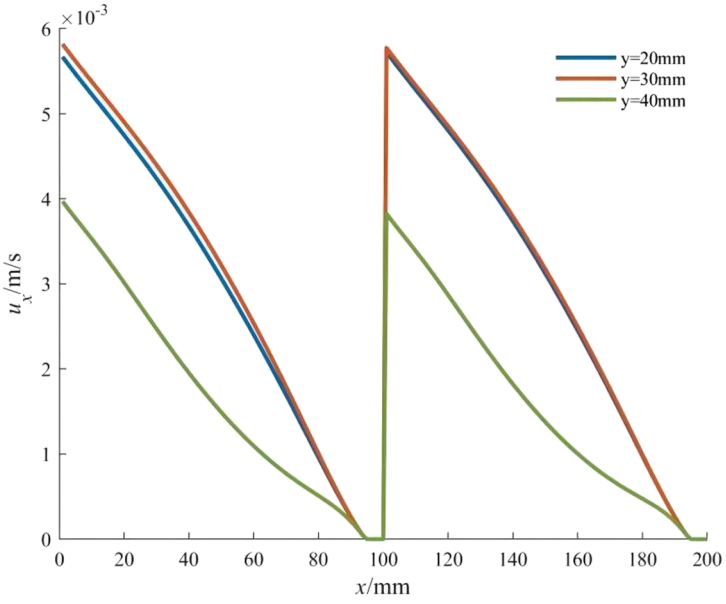

(b)

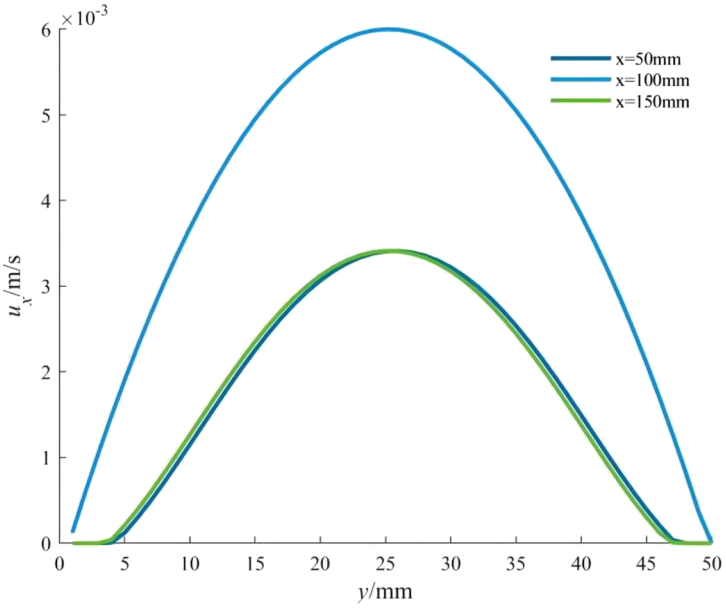

(c)

Figure 5: Simulation results of constant depth variable pitch screw in the *y*–*z*-direction: (a) velocity distribution diagram of a constant depth variable pitch screw, (b) velocity distribution of u_x in the *x*-direction, (c) velocity distribution of u_x in the *y*-direction, (d) velocity distribution of u_y in the *x*-direction, and (e) velocity distribution of u_y in the *y*-direction.

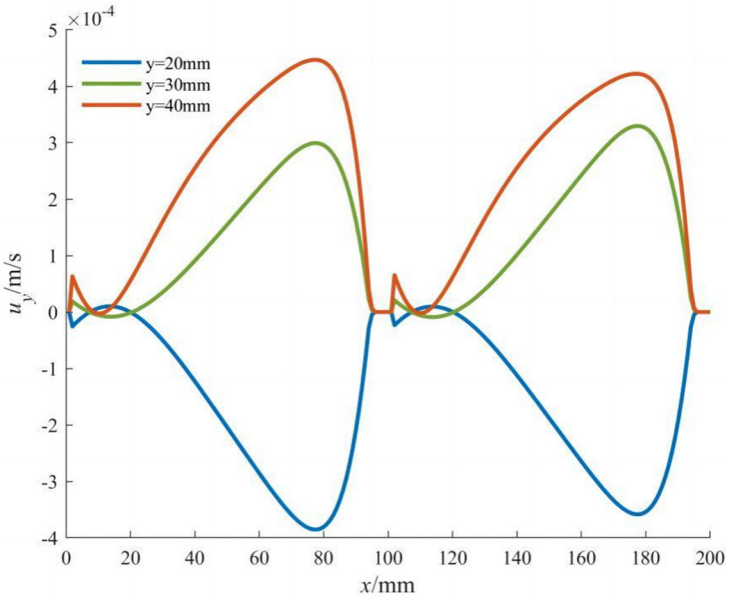

(d)

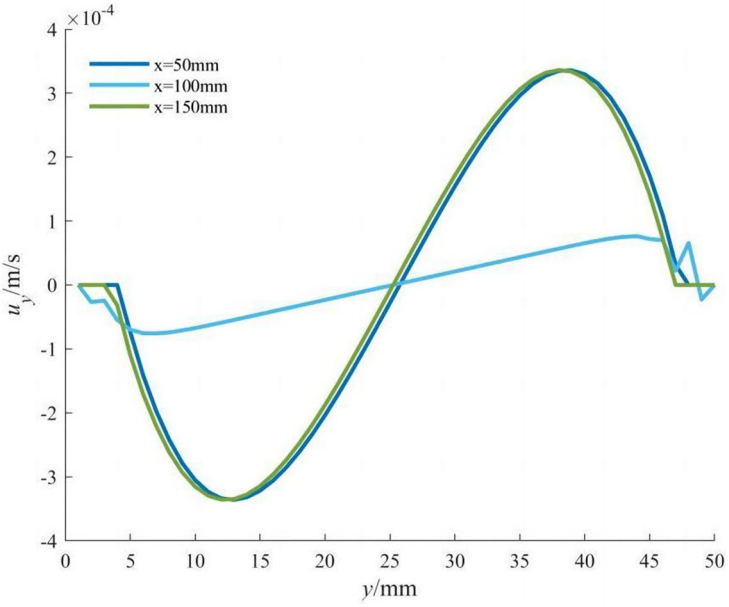

(e)

Figure 5: (*Continued*)

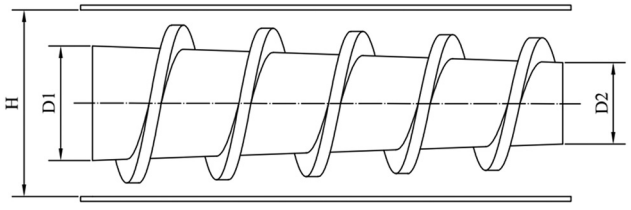

Figure 6: Engineering drawing of variable depth constant pitch screw.

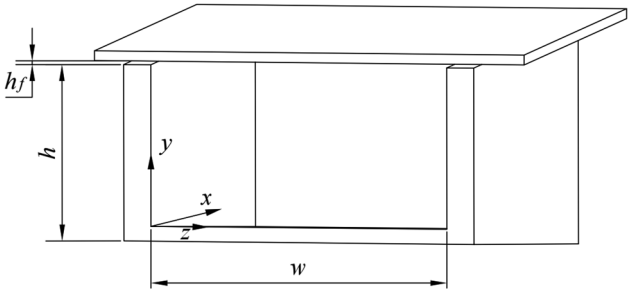

Figure 7: Flow channel of variable depth constant pitch screw.

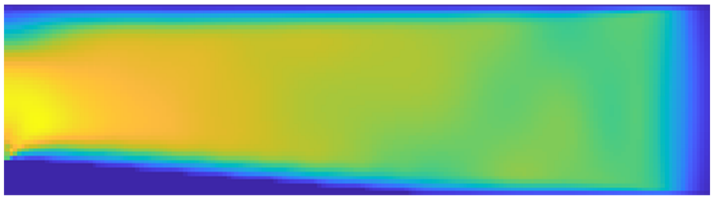

(a)

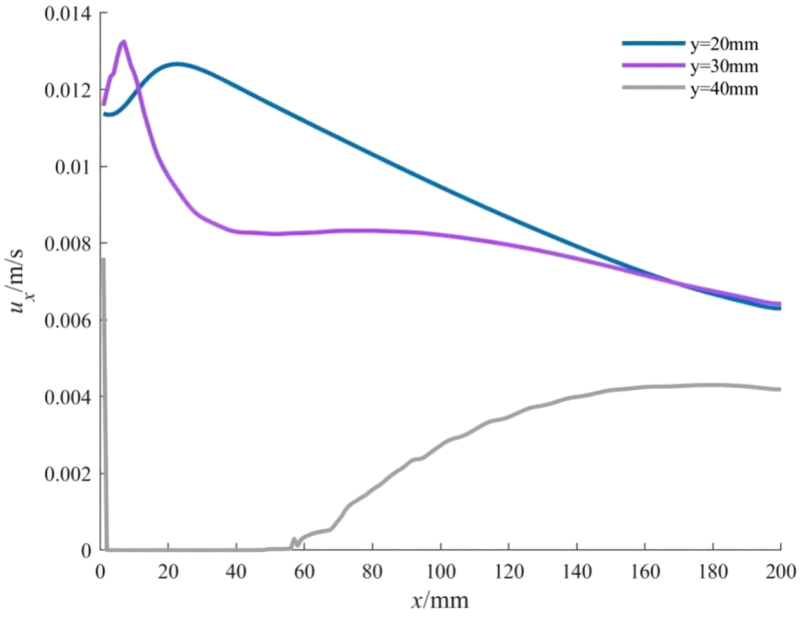

(b)

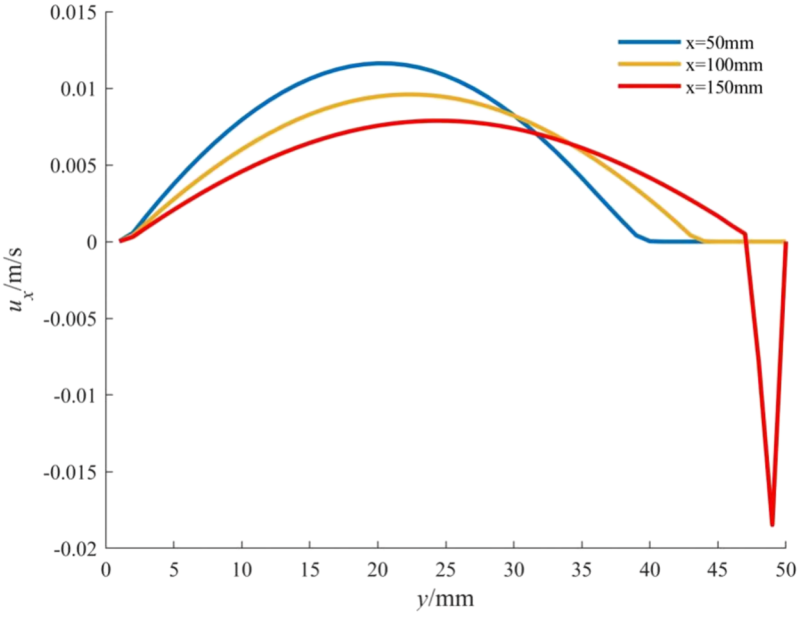

(c)

Figure 8: Simulation results of variable depth constant pitch screw in the *x*–*y*-direction: (a) velocity program of variable depth constant pitch screw, (b) velocity distribution of u_x in the *x*-direction, (c) velocity distribution of u_x in the *y*-direction, (d) velocity distribution of u_y in the *x*-direction, and (e) velocity distribution of u_y in the *y*-direction.

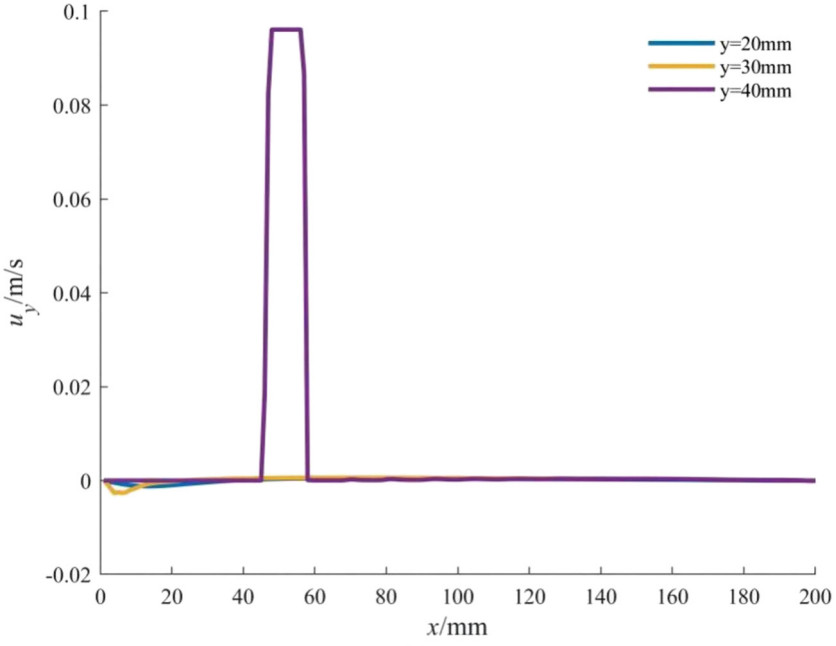

(d)

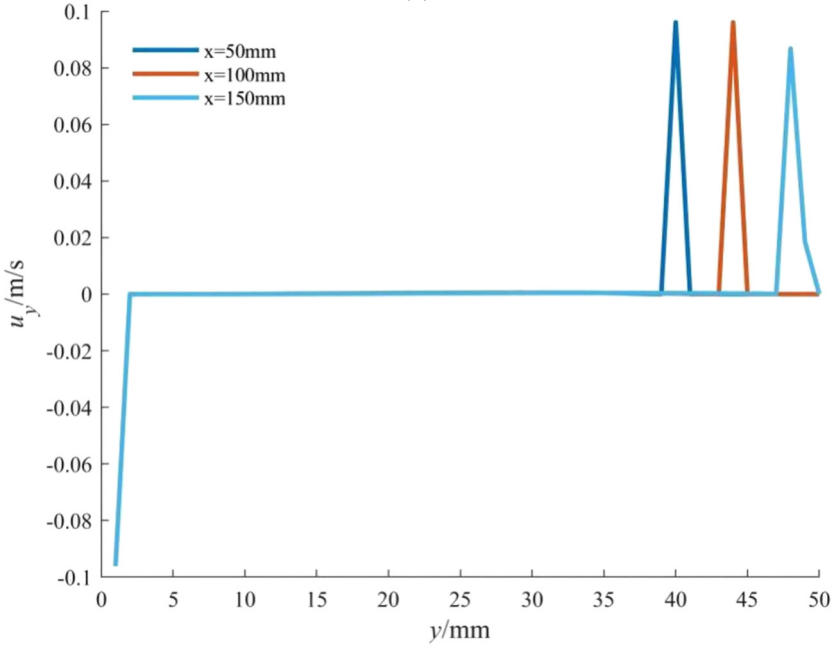

(e)

Figure 8: (*Continued*)

the simulation results in the *x*–*y*-section. The cloud diagram is shown in Figure 5(a). The velocity u_x in the *x*-direction shown in Figure 5(b) presents a similar "N"-shaped change trend, *i.e.*, it first linearly decreases, then suddenly rises, and finally linearly decreases. The graph exhibits identical trends in the two intervals x = 0–100 mm and x = 100–200 mm, as shown in Figure 5(c). It is speculated that the reason for this situation may be due to the overall symmetry of the flow channel. The velocity change trend in the *y*-direction presents a parabolic shape with an opening downward. As shown in Figure 5(d) and (e), the velocity u_y in the *x*-direction and the upper half of the flow channel first decreases, then rises and decreases, and finally rises; the variation pattern of the graphics here is the same as that of u_x. The overall velocity in the *y*-direction shows a trend of first decreasing, then rising, and finally decreasing. The graph is symmetric about the point (y = 25 mm, u_y = 0).

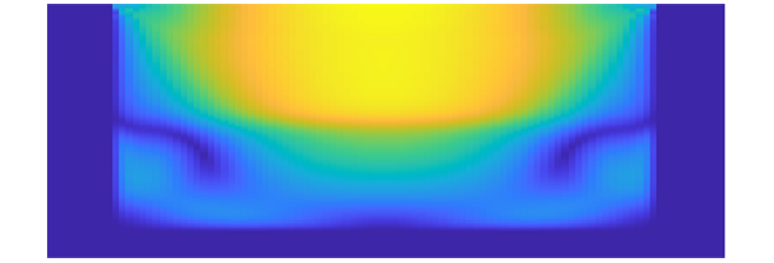

(a)

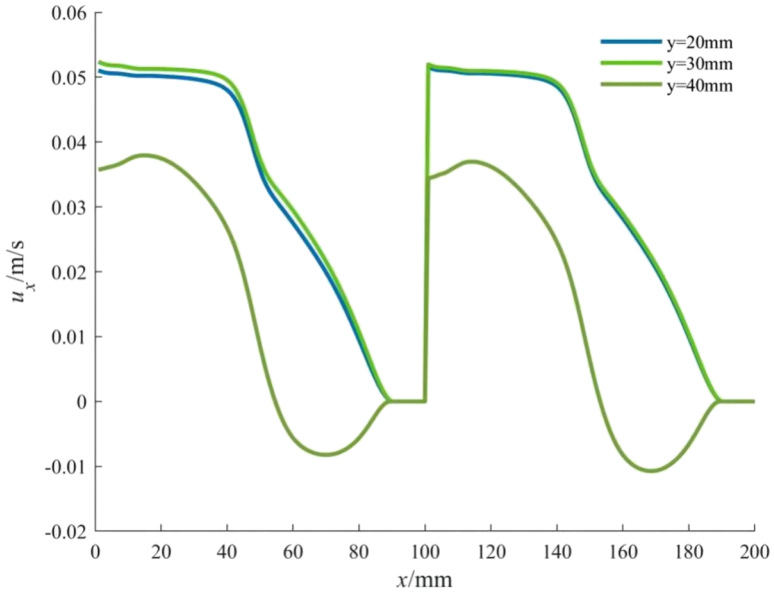

(b)

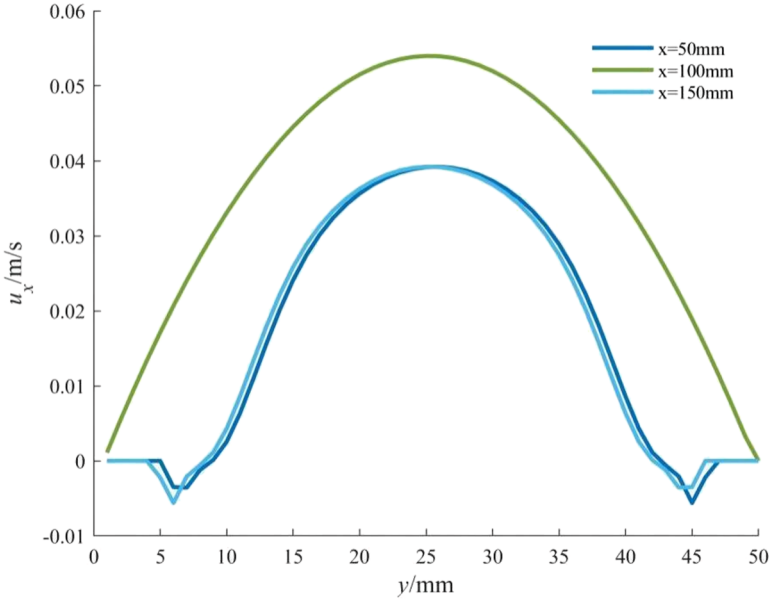

(c)

Figure 9: Simulation results of variable depth constant pitch screw in the *y*–*z*-direction: (a) velocity program of variable depth constant pitch screw, (b) velocity distribution of u_x in the *x*-direction, (c) velocity distribution of u_x in the *y*-direction, (d) velocity distribution of u_y in the *x*-direction, and (e) velocity distribution of u_y in the *y*-direction.

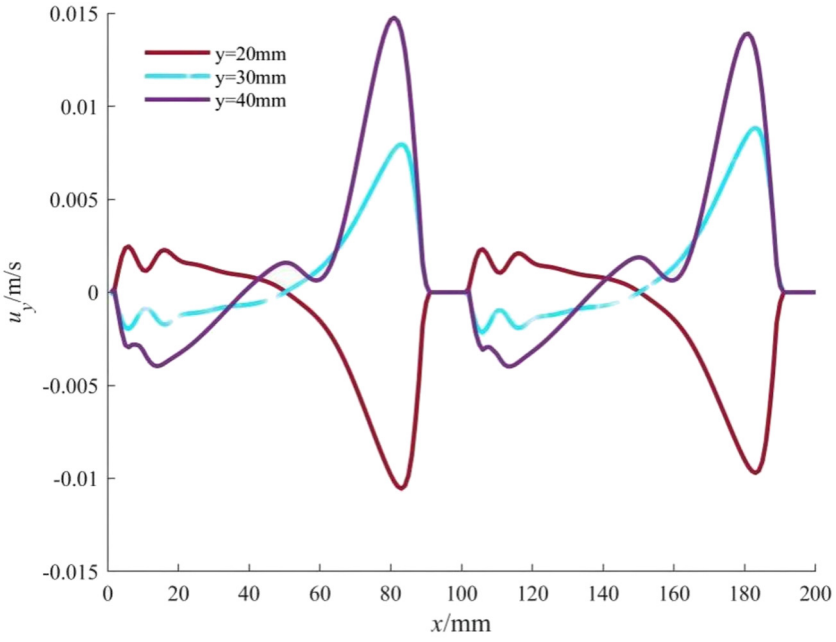

(d)

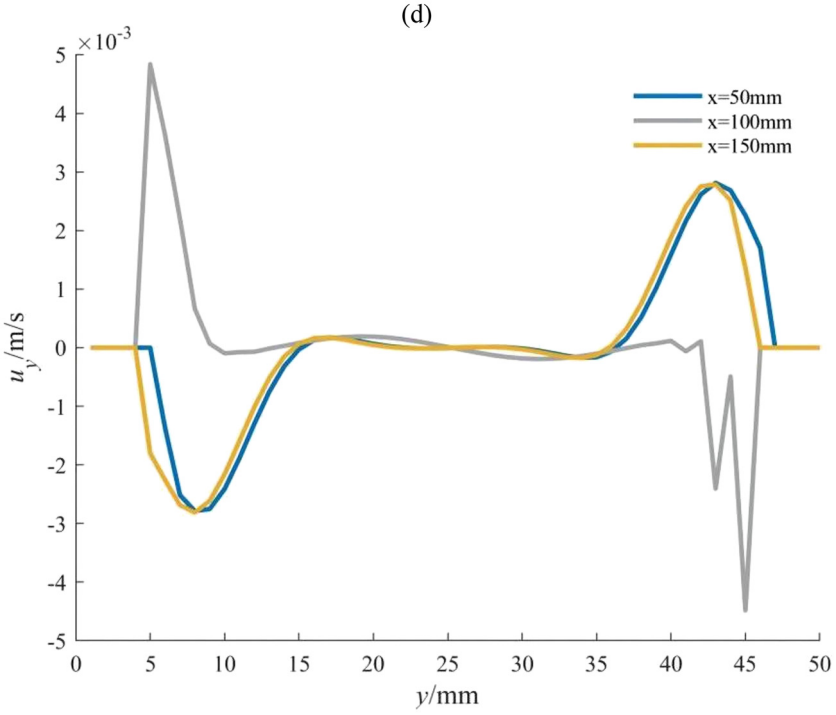

(e)

Figure 9: (*Continued*)

In summary, due to the relatively regular shape of the expanded flow channel of the constant depth variable pitch screw, the impact on the flow of ceramic slurry is not significant and generally presents a form similar to Poiseuille flow.

4.2 Variable depth constant pitch screw

When using a variable depth constant pitch screw, it is not necessary to consider changes in pitch. The structure and the flow channel are shown in Figures 6 and 7. The flow

channel of the screw is rectangular in the x–z-section. Similar to the constant depth variable pitch screw, the flow in two different cross sections will be analyzed to understand the flow mechanism.

When analyzing the flow in the x–y-section with the variable depth constant pitch screw, the inlet velocity is represented as the same as the case in Section 4.1. The cloud diagram is shown in Figure 8(a). It is found that the irregularity of the flow channel has a significant impact on the flow of ceramic paste. As shown in Figure 8(b) and (c), when u_x in the x-direction is involved, the velocity curve shows a trend of first rising and then falling, but in the final part, it only shows an upward trend. The overall velocity change trend in the y-direction is similar to a parabola with an opening downward. As shown in Figure 8(d), u_y in the x-direction tends to decrease first and then increase before y = 40 mm and finally tends to stabilize. However, after y = 40 mm, a maximum value will be generated and then quickly recovers to around 0. In the y-direction, it will first rise, then remain at 0, and then a peak will appear. As can be seen from Figure 8(e), the position of the peak will be delayed as the distance increases.

When analyzing the flow in the y–z-section with the variable depth constant pitch screw, the inlet velocity is represented by a parabola, with a maximum velocity of 1.5 m/s and a minimum velocity of 0 m/s. The value of the inlet velocity here is also selected based on the simulation results in the x–y-section. The cloud diagram is shown in Figure 9(a). The velocity component u_x in the x-direction shown in Figure 9(b) presents a trend of first decreasing, then rapidly rising, and finally decreasing, and u_x in the y-direction shown in Figure 9(c) presents a parabolic shape with an opening downward. As shown in Figure 9(d), u_y in the x-direction is divided into two parts. In the first half of the flow channel, the change presents a trend of first falling and then rising, then falling, and then rising again. Then, repeat the previous change pattern at x = 100 mm. In the y-direction shown in Figure 9(e), it first decreases and then rises, then fluctuates up and down at 0, and then an opposite change occurred after y = 25 mm compared to before.

Compared with the constant depth variable pitch screw, the flow channel of the variable depth constant pitch screw has a greater impact on the flow of ceramic slurry. This is due to the adverse effect of the internal shape of the flow channel of this screw on the flow. In summary, the flow path of the variable depth constant pitch screw has a certain impact on the flow of ceramic slurry. The slope of the lower surface of the flow channel has some adverse effects on the flow of slurry.

4.3 Variable depth variable pitch screw

When using a variable depth variable pitch screw, both the depth and pitch are changing, which is more complex than in the aforementioned situation. The structure and the flow channel are shown in Figures 10 and 11. The flow channel of the screw is an isosceles trapezoid in the x–z-section, similar to the constant depth variable pitch screw. Similar to the first two types of screws, the flow channel should be divided into x–y- and y–z-sections.

When analyzing the flow in the x–y-section of the variable depth variable pitch screw, the inlet velocity is set as the same in the aforementioned two cases. The cloud diagram is shown in Figure 12(a). From this figure, it can be seen that the high-velocity area is significantly compressed. As can be seen from Figure 12(b)–(e), the variation trend of u_x and u_y is similar to and slightly different from the x–y-section of the variable depth constant pitch screw, so the variation rule of its velocity curve will not be described in more detail.

When analyzing the flow in the y–z-section with the variable depth variable pitch screw flow channel, the inlet velocity is represented by a parabola, with a maximum velocity of 0.2 m/s and a minimum velocity of 0 m/s. The

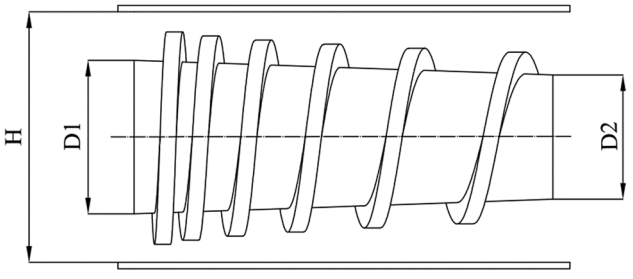

Figure 10: Engineering drawing of variable depth variable pitch screw.

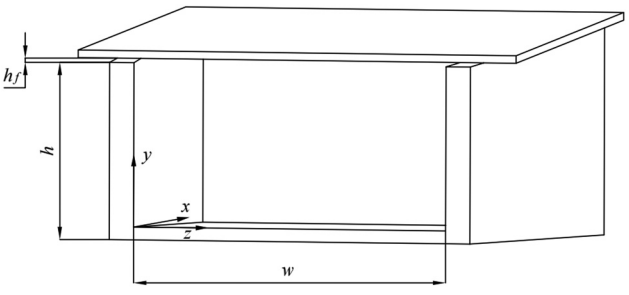

Figure 11: Flow channel of variable depth variable pitch screw.

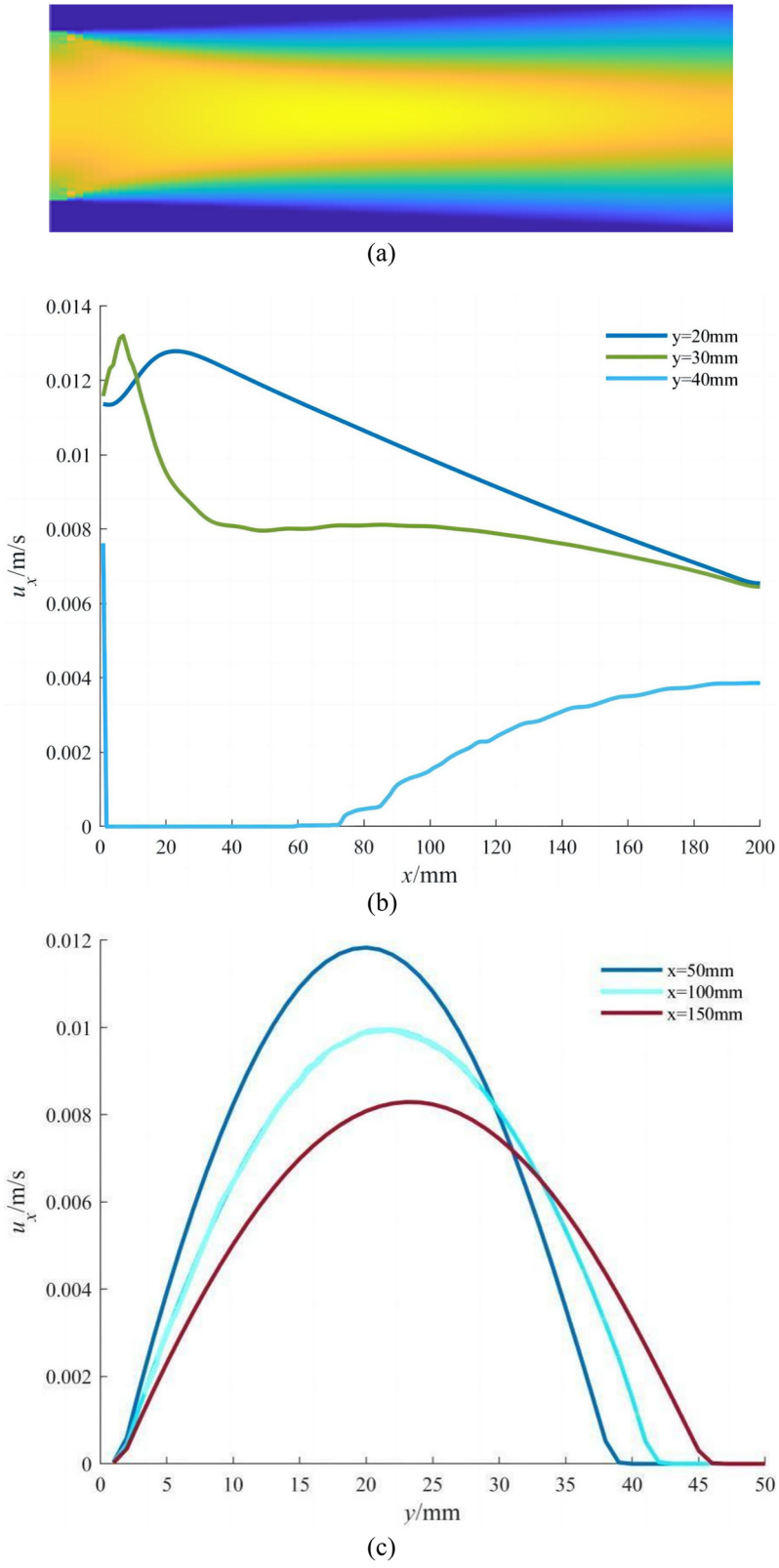

Figure 12: Simulation results of variable depth variable pitch screw in the *x*–*y*-direction: (a) velocity program of variable depth variable pitch screw, (b) velocity distribution of u_x in the *x*-direction, (c) velocity distribution of u_x in the *y*-direction, (d) velocity distribution of u_y in the *x*-direction, and (e) velocity distribution of u_y in the *y*-direction.

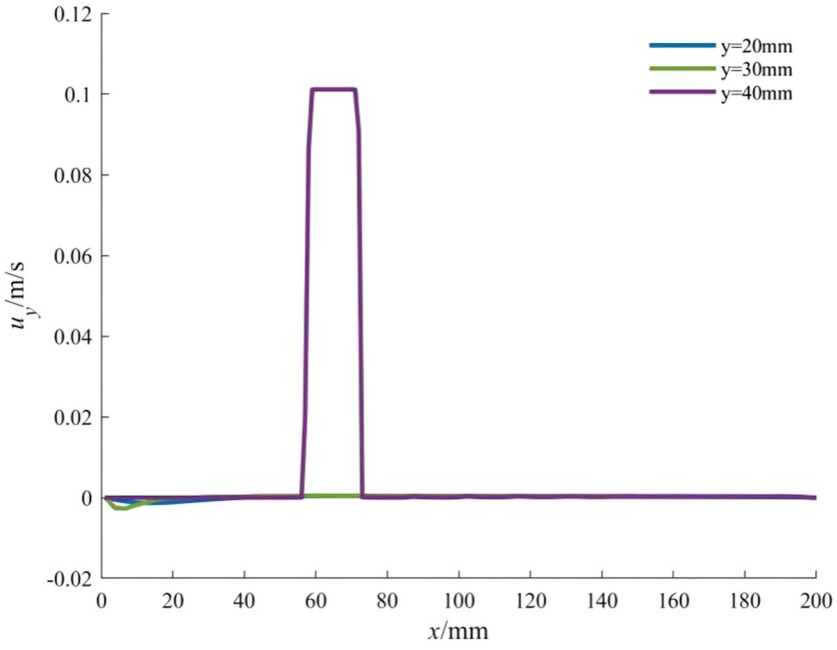

(d)

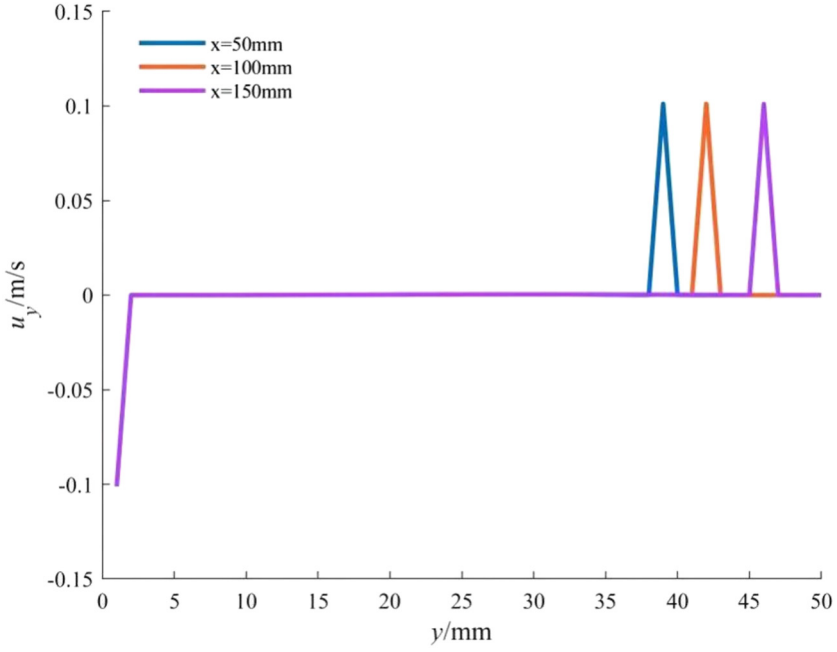

(e)

Figure 12: (*Continued*)

value of the inlet velocity here is determined based on the aforementioned simulation results. The cloud diagram is shown in Figure 13(a). From this figure, it can be seen that the flow channel in this case has a slight impact on the flow of ceramic slurry, and it is not significant for the compression of the notification area. As can be seen from Figure 13(b)–(e), the variation trends of u_x and u_y are similar to and slightly different from the y–z-section of the constant depth variable pitch screw, so we will not expand on them in detail here.

Compared with the two types of screws mentioned earlier, the variable depth variable pitch screw has a significant impact on the flow of ceramic slurry. This is because the internal structure of the flow channel of the

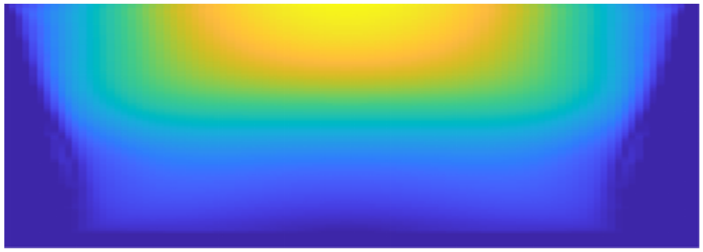

(a)

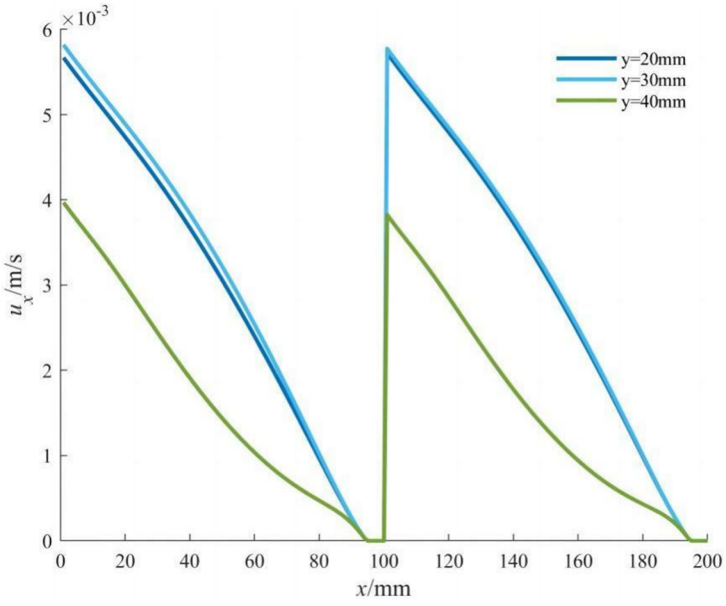

(b)

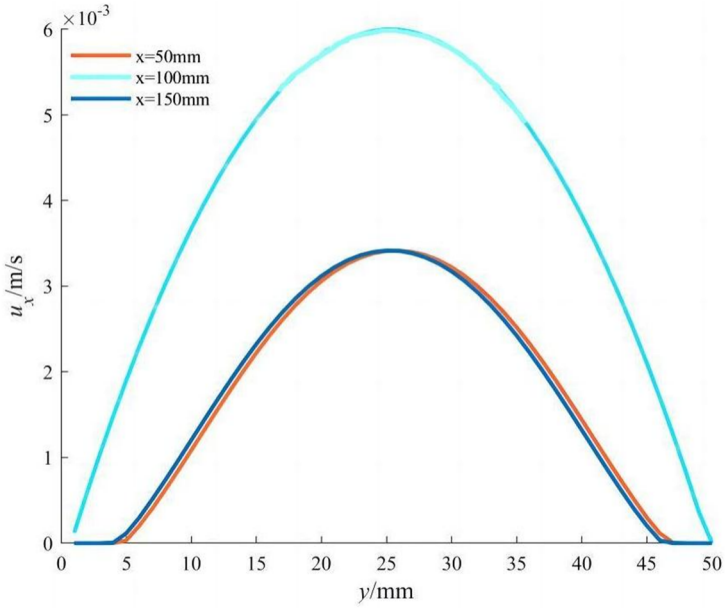

(c)

Figure 13: Simulation results of variable depth variable pitch screw in *y*–*z*-direction: (a) velocity program of variable depth variable pitch screw, (b) velocity distribution of u_x in the *x*-direction, (c) velocity distribution of u_x in the *y*-direction, (d) velocity distribution of u_y in the *x*-direction, and (e) velocity distribution of u_y in the *y*-direction.

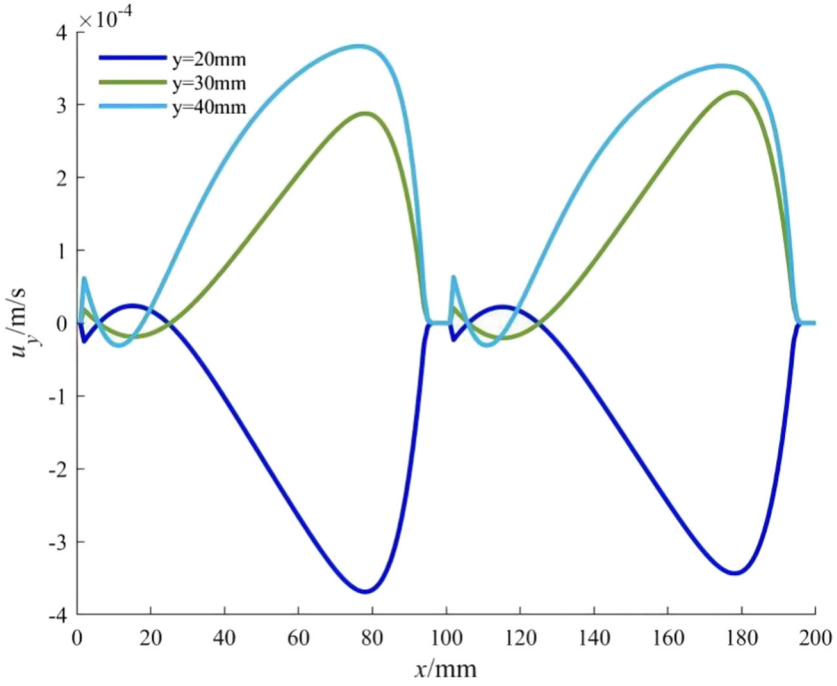

(d)

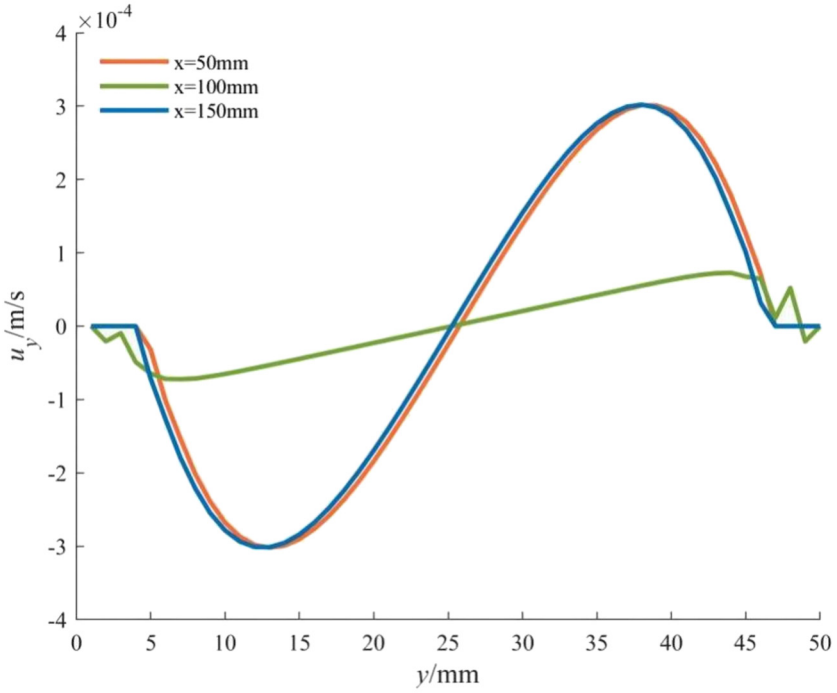

(e)

Figure 13: (*Continued*)

variable depth variable pitch screw is much more complex than the first two, and the adverse effects on the flow are also significant. In summary, the influence of the flow channel of the variable depth variable pitch screw on the ceramic paste is the most significant among the three types of screws.

5 Discussion

This article studies the simulation analysis of ceramic slurry flow after three types of special-shaped screw flow channels are, respectively, expanded in the *x*–*y*-section and *y*–*z*-section.

First, the flow analysis results on the *x*–*y* section of three cases are compared. According to Figures 4, 8, and 12, we can see from its cloud map that the high-velocity area of the variable depth variable pitch screw flow channel accounts for the smallest proportion. In other words, this flow channel has the most significant impact on slurry flow. However, the impact of the other two screw flow channels on slurry flow is not significantly different.

Next, we will compare and discuss the simulation results of the *y*–*z*-section. According to Figures 5, 9, and 13, We can see that in this case, the high-velocity area of the variable depth constant pitch screw channel is the smallest, which means that this screw has the most significant impact on the slurry flow on the *y*–*z*-section. Then, take a look at the constant depth variable pitch screw, whose speed changes are the most regular and traceable. The speed change of the variable depth variable pitch screw is similar to the former.

6 Conclusion

As an AM technology, slurry DIW provides an innovative and effective method for ceramic material forming. To promote the transportation of slurry, a single-screw extruder is selected. The flow channel will change correspondingly when the profiled single-screw extruder is used, which will affect the normal flow and the outlet velocity distribution. In this study, three kinds of profiled single-screw extruders were taken as examples to reveal the basic mechanism of the flow channel obstacles in the profiled single-screw extruders. The LBM is an effective mesoscopic flow analysis method. To improve the stability of non-Newtonian slurry, an LBM for non-Newtonian fluid is proposed.

Based on the obtained velocity program and the speed distribution diagram on the *x*–*y*/*y*–*z*-section, the following conclusions can be summarized, which help select a suitable profiled single-screw extruder.

Combining the flow analysis diagrams of three types of screws, it can be seen that the influence of variable depth variable pitch screw on the flow of ceramic slurry is relatively complex, with more changes in the flow direction. The influence of constant depth variable pitch screw on the flow of ceramic slurry is relatively small, and overall, it shows a trend of Poisson flow.

In summary, to ensure the stability of the slurry transportation process, variable depth variable pitch screws should be avoided as much as possible for the transportation of ceramic slurry.

This article overlooks the occurrence of obstacles in the flow channel. In future work, further research will be conducted on the impact of obstacles generated in the flow channel on the flow of ceramic slurry.

Acknowledgments: This work was supported by Postgraduate Practice Innovation Program of Jiangsu Province (Grant No. SJCX22_1722) and Natural Science Foundation of the Jiangsu Higher Education Institutions of China (Grant No. 22KJB460040).

Funding information: This workwas supported by Postgraduate Practice Innovation Program of Jiangsu Province (Grant No. SJCX22_1722) and Natural Science Foundation of the Jiangsu Higher Education Institutions of China (Grant No. 22KJB460040).

Author contributions: Xu Deng and Weiwei Wu performed the simulations and finished the writing. Shuang Ding reviewed the manuscript. Yanjun Zhang validated the results. Binquan Shi conducted the investigation. The authors applied the SDC approach for the sequence of authors. All authors have accepted responsibility for the entire content of thismanuscript and approved its submission.

Conflict of interest: The authors state no conflict of interest.

Data availability statement: Data sharing is not applicable to this article as no datasets were generated or analysed during the current study.

Reference

[1] Soliman M, Alzahrani G, Alabdualataif F, Eldwakhly E, Alsamady S, Aldegheishem A, et al. Impact of ceramic material and preparation design on marginal fit of endocrown restorations. Materials. 2022;15(16):5592.

[2] Mohr-Weidenfeller L, Kleinholz C, Müller B, Gropp S, Günther-Müller S, Fischer M, et al. Thermal analysis of the ceramic material and evaluation of the bonding behavior of silicon-ceramic composite substrates. J Micromech Microeng. 2022;32(10):105004.
[3] Mamatha S, Biswas P, Das D, Johnson R. Fabrication of complex shaped ceramic articles from 3D printed polylactic acid templates by replication process. Ceram Int. 2019;45(15):19577–80.
[4] Wei HL, Bhadeshia HKDH, David SA, DebRoy T. Harnessing the scientific synergy of welding and additive manufacturing. Sci Technol Weld Join. 2019;24(5):361–6.
[5] Brunello G, Donos N, Sivolella S, Zavan B. Editorial: Advances in additive manufacturing technologies for the production of tissue-engineered bone scaffolds for dental applications. Front Bioeng Biotech. 2022;10:980430.
[6] Ryan KR, Down MP, Hurst NJ, Keefe EM, Banks CE. Additive manufacturing (3D printing) of electrically conductive polymers and polymer nanocomposites and their applications. eScience. 2022;2(4):365–81.
[7] Duda T, Raghavan LV. 3D metal printing technology: the need to re-invent design practice. Ai Soc. 2018;33(2):241–52.
[8] Kabouraki E, Melissinaki V, Yadav A, Melninkaitis A, Tourlouki K, Tachtsidis T, et al. High laser induced damage threshold photoresists for nano-imprint and 3D multi-photon lithography. Nanophotonics-Berlin. 2021;10(14):3759–68.
[9] Murphy RD, Garcia RV, Oh SJ, Wood TJ, Jo KD, de Alaniz JR, et al. Tailored polypeptide star copolymers for 3D printing of bacterial composites Via direct ink writing. Adv Mater. 2022;35(3):e2207542.
[10] Ma ZY, Liu JB, Zhang XD, Deng RX, Lu S, Wu YH, et al. Flexible surfaces prepared through direct ink writing with drag reduction and antifouling. Colloid Surf A. 2022;655:130223.
[11] Ma SQ, Liu XH, Fu S, Zhao SJ, He PG, Duan XM, et al. Direct ink writing of porous SiC ceramics with geopolymer as binder. J Eur Ceram Soc. 2022;42(15):6815–26.
[12] Tu YQ, Hassan A, Siadat A, Yang GL, Chen ZW. Numerical simulation and experimental validation of deposited corners of any angle in direct ink writing. Int J Adv Manuf Technol. 2022;123(1–2):559–70.
[13] Gu SH, Ji HY, Liang K, Ji YL. Chitin nanocrystal based aqueous inks for 3D printing via direct ink writing. J Elastom Plast. 2022;54(6):922–36.
[14] Shi LH, Xiao XZ, Liu TT, Liao WH, Kong LH. Design and performance of a flexible broadband metamaterial absorbing structure fabricated based on the direct ink writing 3D printing. J Phys D: Appl Phys. 2022;55(45):455001.
[15] Liu N, Sun XH, Chen Z, Xu ZK, Dai N, Shi GH, et al. Direct ink writing of dense alumina ceramics prepared by rapid sintering. Ceram Int. 2022;48(20):30767–78.
[16] Wu WF, Zhang Z, Peng CY, Li XW, Yang YF, Lei WW. Refreshed internal working characteristics of the single screw compressor based on experimental investigation. Int J Refrig. 2022;143:118–25.
[17] Fujimoto T, Sei A, Taniwaki T, Okada T, Yakushiji T, Mizuta H. Pedicle screw diameter selection for safe insertion in the thoracic spine. Eur J Orthop Surg Traumatol. 2012;22(5):351–6.
[18] Liu XM, Huang JC, Wang GD, Lan SH, Wang HS, Pan CW, et al. Anterior titanium plate plus screw of square area combined with posterior column screw for the treatment of fracture of acetabulum involving square area. Int J Clin Exp Med. 2016;9(1):108–19.
[19] Roebke AJ, Roebke LJ, Goyal KS. Fracture gap reduction with variable-pitch headless screws. J Hand Surg. 2018;43(4):385.e1–8.
[20] Wu WF, Zhang Z. Development of single screw compressor technologies and their tendency. P I Mech Eng E-J Pro. 2022;236(2):738–51.
[21] David AJ, Justin RS, William CR, Naik UP, Beris AN. An impedance model for blood flow in the human arterial system Part I: Model development and MATLAB implementation. Comput Chem Eng. 2010;35(7):1304–16.
[22] Ponalagusamy R, Manchi R. A four-layered model for flow of non-Newtonian fluid in an artery with mild stenosis. Sadhana-Acad P Eng S. 2019;44(7):1–14.
[23] Siddiqa S, Begum N, Hossain MA, Gorla RSR. Natural convection flow of a two-phase dusty non-Newtonian fluid along a vertical surface. Int J Heat Mass Transf. 2017;113:482–9.
[24] Bouzit F, Bouzit M, Mokeddem M. Study of the rheological behaviour and the curvature radius effects on a non-newtonian fluid flow in a curved square duct. Int J Eng Res Afr. 2022;6482:225–38.
[25] Bisht M, Patil DV. Assessment of multiple relaxation time-lattice Boltzmann method framework for non-Newtonian fluid flow simulations. Eur J Mech B-fluid. 2021;85:322–34.
[26] Khabazi NP, Taghavi SM, Sadeghy K. Peristaltic flow of Bingham fluids at large Reynolds numbers: a numerical study. J Non-Newton Fluid. 2016;227:30–44.
[27] Avila M, Barkley D, Hof B. Transition to turbulence in pipe flow. Annu Rev Fluid Mech. 2023;55:575–602.
[28] Zhu J, Yu JT, Wu YC, Chao YH, Wu PW, Lu LJ, et al. Engineering 3D-printed aqueous colloidal ceramic slurry for direct ink writing. Green Chem Eng. 2023;4(1):73–80.
[29] Tang J, Chang HT, Guo XT, Liu M, Wei YQ, Huang ZR, et al. Preparation of photosensitive SiO2/SiC ceramic slurry with high solid content for stereolithography. Ceram Int. 2022;48(20):30332–7.
[30] Almaneea A. Numerical study on heat and mass transport enhancement in MHD Williamson fluid via hybrid nanoparticles. Alex Eng J. 2022;61(10):8343–54.
[31] Rahman S, Khan N, Hayat T, Ahmad B. Global regularity for MHD Sisko fluid in annular pipe. Anal Math Phys. 2017;7(4):417–35.
[32] Luo LS. Theory of the lattice Boltzmann method: Lattice Boltzmann models for nonideal gases. Phys Rev E. 2000;62(4):4982–96.
[33] Jianhua L, Haifeng H, Baochang S, Guo ZL. Immersed boundary lattice Boltzmann model based on multiple relaxation times. Phys Rev E. 2012;85:016711.
[34] Zou QS, He XY. On pressure and velocity boundary conditions for the lattice Boltzmann BGK model. Phys Fluids. 1997;9(6):1591–8.